Earth Planet. Sci. Lett. 690 (2026) 120177

Contents lists available at ScienceDirect

Earth and Planetary Science Letters

journal homepage: www.elsevier.com/locate/epsl

Cyclic water-sediment supply coarsens the temporal resolution of fluvio-deltaic strata

Youwei Wang [a,b,c,*], Vamsi Ganti [b], Ajay B. Limaye [c], Kyle M. Straub [d]

[a] State Key Laboratory of Lithospheric and Environmental Coevolution, Institute of Geology and Geophysics, Chinese Academy of Sciences, Beijing, China
[b] Department of Geography, University of California Santa Barbara, Santa Barbara, CA, USA
[c] Department of Environmental Sciences, University of Virginia, Charlottesville, VA, USA
[d] Department of Earth and Environmental Sciences, Tulane University, New Orleans, LA, USA

ARTICLE INFO

Editor: J.P. Avouac

Keywords:
Compensation timescale
External forcing
Stratigraphic temporal resolution
Surface roughness
Signal preservation
Sediment mass extraction

ABSTRACT

Fluvio-deltaic deposits archive environmental change, but internal depositional dynamics can modify or erase signals before preservation. Whether a signal survives the stratigraphic filter depends in part on its duration: signals with periods shorter than the time required for a system to smooth its own uneven topography tend to be lost, whereas longer-period signals are more readily preserved. This smoothing timescale, or compensation timescale (T_c), is well constrained under steady conditions, but how it responds to external forcing remains unclear. Here we combine physical and numerical experiments spanning a range of forcing amplitudes and periods in input sediment-to-water discharge ratio, using a sediment mass-extraction framework to define dynamically equivalent measurement positions across experiments. We show that cyclic forcing increases T_c by as much as fourfold relative to unforced controls. Under fast forcing, intermediate amplitudes produce the longest T_c, whereas weak and strong forcing amplitudes yield values within 30% of the control. Under slow forcing, T_c increases more monotonically with amplitude, reaching two- to threefold above control at the highest amplitudes tested. Basin-scale topographic roughness, rather than local channel depth, is the strongest predictor of T_c across both forcing regimes ($r = 0.81$–0.89, $p < 0.001$). These results show that forcing itself modifies the temporal resolution of the stratigraphic archive, so the stratigraphic record is not a passive filter with a fixed cutoff; instead, its temporal resolution coevolves with the amplitude and period of the forcing it records.

1. Introduction

A central challenge in Earth science is determining which environmental changes are faithfully recorded in sedimentary strata and which are lost or distorted before preservation (Allen, 2008; Romans et al., 2016; Tofelde et al., 2021). This challenge is fundamental because the temporal resolution at which strata become reliable archives of environmental change remains insufficiently constrained (Sadler, 1981; Straub et al., 2020). Stratigraphic patterns reflect both external forcing and internal (autogenic) dynamics such as channel migration and avulsion (Hajek and Straub, 2017). Autogenic processes can obscure, mimic, or destroy signals of external forcing (Burgess and Duller, 2024; Griffin et al., 2023; Jerolmack and Paola, 2010), making the timescale at which strata become reliable environmental archives a critical but poorly constrained quantity.

The temporal resolution of the stratigraphic archive depends on how sedimentation varies across timescales. At short timescales, sedimentation is spatially heterogeneous and dominated by autogenic dynamics, with the characteristic duration of this heterogeneity varying as a function of surface roughness and aggradation rate (Ganti et al., 2014; Hajek and Straub, 2017; Sheets et al., 2002). Over longer timescales, depositional systems tend toward more ordered sedimentation (Jerolmack and Sadler, 2007) through compensational stacking, a tendency for sedimentation to preferentially fill topographic lows, which progressively smooths surface relief and brings local sedimentation rates into alignment with the long-term basin-wide average (Straub et al., 2009; Wang et al., 2011). This behavior has been documented across fluvial, deltaic, debris flow, glaciomarine, and deepwater systems (Esposito et al., 2018; Pederson et al., 2015; Tasistro-Hart et al., 2025; Trampush et al., 2017; Wang et al., 2023). The resulting framework has been applied to problems ranging from paleoclimate signal propagation to geomorphic hazard assessment and outcrop characterization

* Corresponding author.
E-mail address: youweiwang@mail.iggcas.ac.cn (Y. Wang).

https://doi.org/10.1016/j.epsl.2026.120177
Received 7 November 2025; Received in revised form 5 April 2026; Accepted 8 June 2026
Available online 13 June 2026

(Bernhardt et al., 2017; Hajek and Wolinsky, 2012; McLain et al., 2024; Romans et al., 2016), motivating efforts to quantify the timescale over which compensation is achieved.

The compensational timescale (T_c) provides a quantitative measure of this temporal resolution. Defined as the duration required for local sedimentation patterns to converge with the long-term aggradation rate (Wang et al., 2011), T_c marks a threshold: below it, sedimentation is dominated by autogenic dynamics; above it, depositional patterns increasingly reflect external controls (Hajek and Straub, 2017; Straub et al., 2009)—meaning T_c sets the minimum timescale at which environmental signals are more likely to be detected in the stratigraphic record (Foreman and Straub, 2017; Griffin et al., 2023). This threshold is consistent with the well-documented decrease in apparent sedimentation rates with increasing measurement duration (the Sadler effect), where the break in scaling occurs at timescales comparable to T_c estimated from field data (Jerolmack and Sadler, 2007; Straub et al., 2020). Signal preservation above T_c is not guaranteed, however: forcing amplitude also plays an important role (Toby et al., 2019a, 2022; Wang et al., 2021), and autogenic dynamics can generate organized periodicities that complicate signal detection even at longer timescales (Burgess and Duller, 2024).

Most estimates of T_c assume steady forcing: constant sediment supply and stable or monotonically changing base level. Under these conditions, T_c is typically approximated as the ratio of characteristic topographic relief to the long-term aggradation rate (Straub and Wang, 2013; Wang et al., 2011). Natural systems, however, exhibit multi-scale variability in both sediment supply and base-level change (Blum and Törnqvist, 2000; Dong et al., 2023; Kim and Paola, 2007), which can amplify topographic relief through incision during periods of reduced sediment supply or base-level fall. Numerical experiments show that cyclic fluctuations in sediment and water supply can delay the onset of compensational stacking by a factor of up to 2.6 relative to steady conditions (Wang et al., 2011). In models of deep-water fans, autogenic processes further generate cyclical stacking patterns that mask external signals, particularly at longer periods (Burgess et al., 2019; Burgess and Duller, 2024). Whether and how cyclic forcing systematically modifies T_c, and thus the timescale at which paleoenvironmental signals become detectable, remains unresolved.

We test the hypothesis that cyclic water-sediment forcing extends the compensation timescale by amplifying surface roughness, expressed as either local roughness (maximum channel depth) or regional roughness (persistent along-strike differences in depositional thickness). Using paired physical and numerical experiments with cyclic variations in sediment-to-water discharge input, we isolate the effects of forcing period and amplitude on both roughness metrics and T_c. Section 2 describes the experimental setup and analysis methods; Section 3 presents the results; Section 4 interprets the governing mechanisms and implications for stratigraphic signal preservation; and Section 5 summarizes the principal conclusions.

2. Materials and methods

2.1. Physical deltaic experiments

Delta experiments were conducted in the Tulane Delta Basin (TDB) and included one control run under steady forcing and multiple runs (n = 5) with cyclic sediment-to-water discharge (Q_s/Q_w). In all experiments, water ($Q_{w0} = 1.7 \times 10^{-4}$ m^3/s) and sediment (mean mass flux Q_{s0} = 3.9×10^{-4} kg/s) were mixed and fed from a fixed upstream-corner inlet, and sea level rose at a constant rate of r_{SL} = 0.25 mm/h, measured at submillimeter-scale precision, resulting in delta progradation toward a downstream weir (Fig. 1a). The sediment mixture was cohesive, with grain sizes from 1 to 1000 μm (D_{50} = 67 μm), following Hoyal and Sheets (2009). The basin measured 4.2 m long, 2.8 m wide, and 0.65 m deep (Fig. 1a). Topography was scanned hourly on a 5 mm horizontal grid with <1 mm vertical resolution.

Each experiment included a steady-state interval lasting 50 to 140 h; the runtime with cyclic forcing was typically 490 h, except TDB-16–3a (245 h). The control run (TDB-12–1) maintained constant Q_w, Q_s, and r_{SL} throughout, resulting in sustained aggradation and a nearly stationary shoreline (Straub et al., 2015). Previous research estimated a compensational timescale (T_{c0}) of 49 h and a corresponding compensational depth (H_{c0}; calculated as $T_{c0} \times r_{SL}$) of 12.3 mm at a radial distance of 0.4 m from the inlet (Toby et al., 2019a).

In forced runs, Q_s/Q_w varied cyclically, with different periods (P) and amplitudes (A). We classified runs relative to T_{c0}: experiments with $P = 2T_{c0}$ were designated as *slow forcing*, while those with $P = 0.5T_{c0}$ were designated as *fast forcing* (Table 1). Slow-forcing experiments included TDB-16–2, TDB-16–3b and TDB-20–1, while fast-forcing experiments included TDB-16–1 and TDB-16–3a (Straub, 2025; Toby et al., 2019a). We listed these runs in order of increasing forcing amplitude, which ranged from 0.075 to 0.6 of the steady-state mean Q_s/Q_w.

2.2. Numerical fluvial experiments

We analyzed numerical experiments simulating fluvial channel-belt

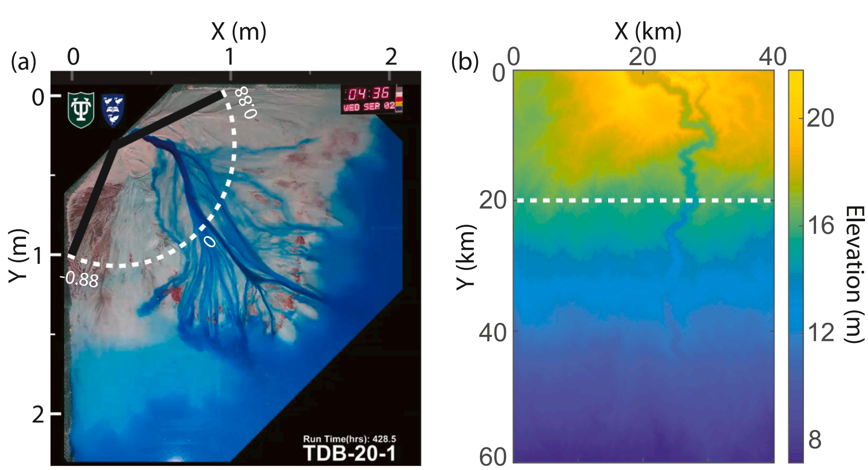

Fig. 1. Setup of physical and numerical experiments. (a) Overhead view of a delta in the Tulane Delta Basin (TDB), shown by a snapshot of surface topography from TDB-20–1 at t = 428.5 h; blue color denotes active water. The basin is 4.2 m long by 2.8 m wide; the sediment-water inlet is at the upper left corner. (b) Overhead view of modeled topography from a numerical experiment (Scenario A40P10 at t = 20 kyr) using the Karssenberg and Bridge (2008) model; the domain is 60 × 40 km. White dashed lines in (a) and (b) mark example cross-stream transect locations used for subsequent analyses.

Table 1
Key parameters for all the physical and numerical experiments used in this study.

	Regimes	Experiments	Period (P)	Amplitude of Q_s/Q_w change (A_Q)	Amplitude of sea level change (A_R)
Physical-control run	Steady	TDB-12-1	0	0	0
Physical-Q_s/Q_w forcing	Fast forcing	TDB-16-1	24.5 h	0.075	0
		TDB-16–3a	24.5 h	0.3	0
	Slow forcing	TDB-16–2	98 h	0.075	0
		TDB-16–3b	98 h	0.15	0
		TDB-20–1	98 h	0.6	0
Numerical-control run	Steady	NC	0	0	0
Numerical-Q_s/Q_w forcing	Fast forcing	A10P1.25	1.25 kyr	0.1	0
		A20P1.25	1.25 kyr	0.2	0
		A40P1.25	1.25 kyr	0.4	0
	Slow forcing	A5P10	10 kyr	0.05	0
		A10P10	10 kyr	0.1	0
		A20P10	10 kyr	0.2	0
		A40P10	10 kyr	0.4	0

evolution using the Karssenberg and Bridge (2008) model, including previously published runs (Wang et al., 2021) and new experiments (Wang, 2025). The model resolves basin-scale sediment transport, erosion, and deposition in alluvial settings, with channel belts treated as the fundamental geomorphic unit. All runs utilized an identical domain: a 60 × 40 km rectangular basin discretized into 200 m × 200 m cells with an initial slope (S_0) of 0.00011 (Fig. 1b).

The control run (Scenario NC) maintained constant water discharge ($Q_{w0,n} = 7.9 \times 10^{10}$ m^3/yr), volumetric sediment supply ($Q_{s0,n} = 1.0 \times 10^6$ m^3/yr), and sea-level rise rate (0.0004 m/yr). These values were chosen to maintain a balance between sedimentation and the rate of relative sea-level rise, yielding sustained aggradation consistent with long-term rates estimated from alluvial stratigraphy (Abels et al., 2012; Wang et al., 2024). Previous research estimated a compensational timescale ($T_{c0,\ n}$) of 2.0 kyr at a distance of 20 km from the basin inlet (Wang et al., 2021).

Seven additional runs imposed cyclic variations in Q_s/Q_w with different periods (P) and amplitudes (A). As in the physical experiments, numerical simulations were categorized as *slow forcing* ($P = 3.3T_{c0,\ n}$) and *fast forcing* ($P = 0.4T_{c0,\ n}$) (Table 1). Slow-forcing experiments include runs A5P10, A10P10, A20P10, and A40P10; fast-forcing experiments comprise A10P1.25, A20P1.25, and A40P1.25 (Wang et al., 2021; Wang, 2025), listed in order of increasing amplitude (A). The forcing amplitude varied from 0.05 to 0.4 of the steady-state mean Q_s/Q_w.

2.3. Data analysis

2.3.1. Transect selection using the mass-extraction parameter (χ)

We analyzed the temporal changes in depositional surface topography along cross-stream transects for all experiments. Because different forcing regimes modify progradation distances and sediment partitioning, a fixed transect represents a different relative position within the sediment-routing system across experiments (Paola and Martin, 2012; Strong and Paola, 2008). We therefore used the mass extraction parameter χ (Paola and Martin, 2012; Strong and Paola, 2008) to select dynamically equivalent measurement positions across experiments. χ quantifies the dimensionless fraction of supplied sediment mass deposited upstream of a given location, based on cumulative mass balance.

For a radial distance R from the inlet in the physical experiments,

$$\chi(R) = \sum (\Delta Z(i) \ \times A_{cell} \times \ (1 \ - \ \varphi(R)) \ \times \ \rho_s) \Big/ (Q_{s0} \times \ T) \tag{1}$$

where the summation extends over all grid cells i within R; $\Delta Z(i)$ is the net elevation change over the experiment, A_{cell} the cell area (25 mm^2 in physical experiments), $\varphi(R)$ spatially-varying deposit porosity, ρ_s grain density, Q_{s0} mean sediment mass feed rate, and T the experiment duration. In physical experiments, $\varphi(R)$ varies with distance following the empirical relationship of Straub et al. (2015).

The numerical model (Karssenberg and Bridge, 2008) tracks sediment in bulk volume (solid grains plus pore space) with a spatially uniform implicit porosity. Thus, $(1 - \varphi)$ and ρ_s appear identically in numerator and denominator of Eq. (1) and cancel, yielding

$$\chi(x) = \sum (\Delta Z(i) \ \times A_{cell}) \Big/ (Q_{s0} \times \ T) \tag{2}$$

where A_{cell} is 40,000 m^2 in numerical experiments. Here, $\chi(x)$ denotes the cumulative bulk volume deposited upstream of downstream distance x, normalized by total bulk volume supplied.

For each experiment, we computed χ as a function of R (physical experiments) or x (numerical experiments), yielding monotonic $\chi(R)$ or $\chi(x)$ curve increasing away from the source. We define χ_{max} as the 99th percentile of the distribution, which suppresses noise from isolated cells at the distal fringe while faithfully capturing the bulk sediment retention. Hence, χ_{max} represents the fraction of supplied sediment retained within the delta plain; $1 - \chi_{max}$ is the bypass fraction to deep water. We extracted cross-stream topographic transects at χ positions that avoid both near-inlet boundary effects and marine-fringing zone, where poor channelization and high measurement noise degrade topographic signals. Practically, we analyzed transects within $0.25\chi_{max} \le \chi \le 0.5\chi_{max}$; results were insensitive to the choice of this window.

2.3.2. Estimation of the compensational timescale (T_c)

We estimated T_c using the σ_{ss} framework (Wang et al., 2011; Fig. 2), which quantifies the deviation of local sedimentation rates along a cross-stream transect from the long-term aggradation rate:

$$\sigma_{ss}(T) = \left\{ \int_0^L \left[\frac{r(T;x)}{\widehat{r}(x)} - 1 \right]^2 dL \right\}^{1/2} \tag{3}$$

where $r(T;x)$ is the mean deposition rate at position x over time window T, L is transect length, and $\widehat{r}(x)$ is the long-term aggradation rate at position x (Wang et al., 2011). The subscript "ss" refers to sedimentation-to-subsidence; σ_{ss} is a root-mean-square departure from unity rather than a conventional standard deviation, and we retain the notation for consistency with prior work (Straub et al., 2009; Wang et al., 2011).

Empirically, σ_{ss} decreases with increasing T following a power law (Straub et al., 2009; Wang et al., 2011):

$$\sigma_{ss} = a' T^{-\kappa} \tag{4}$$

where a' is a coefficient and κ is the compensation index. In log-log space, Eq. (4) becomes:

$$\log\,(\sigma_{ss}) = \log(a') - \kappa \log\,(T) \tag{5}$$

so that the slope of the linear relationship equals $-\kappa$. This slope typically exhibits two regimes separated by a break (Fig. 2b). At short time windows, the slope $-\kappa_s$ reflects autogenic depositional patterns: $\kappa_s < 0.5$ indicates anti-compensational stacking, $\kappa_s = 0.5$–0.75 indicates random stacking, and $\kappa_s > 0.75$ indicates compensational stacking (Straub and Wang, 2013). At long time windows, the slope steepens toward $-\kappa_l \approx -1$, indicating deterministic basin filling governed by available accommodation (Wang et al., 2011). The compensational timescale T_c is defined as the time window at which this slope break occurs, marking

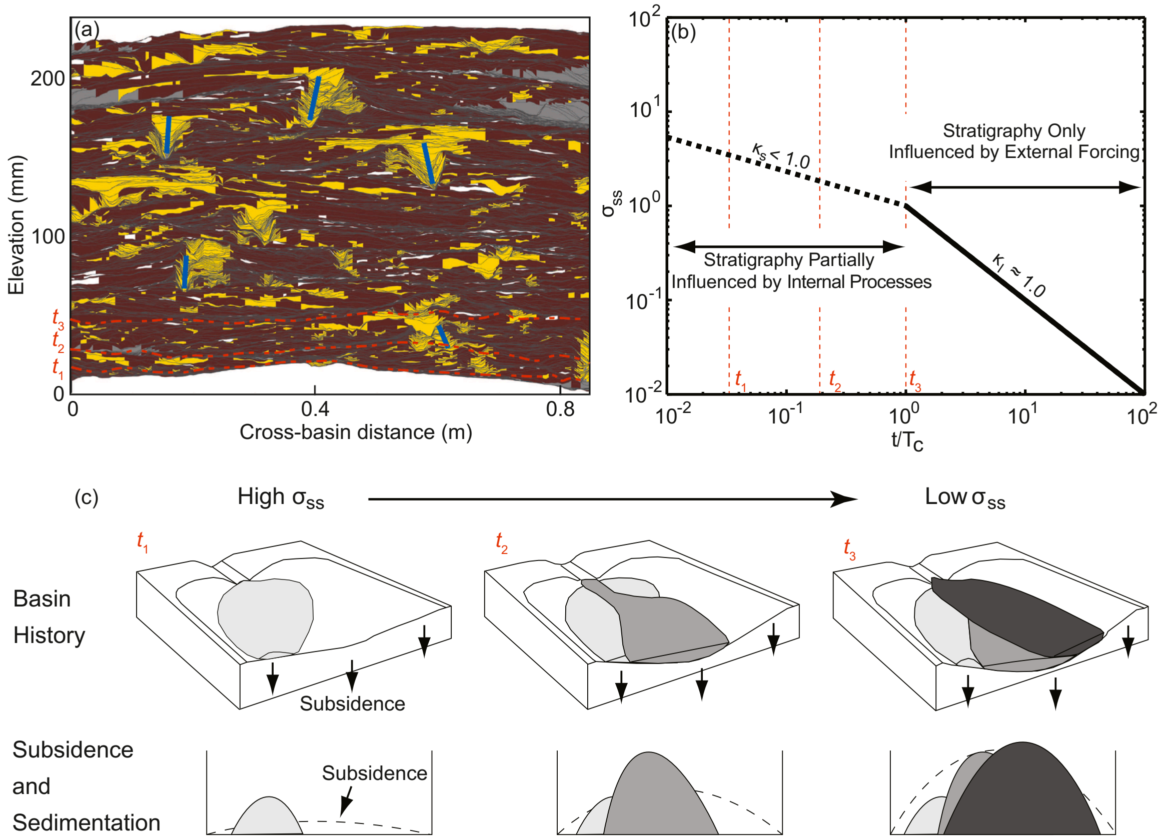

Fig. 2. Illustration of compensational stacking. (a) Synthetic strata of channel (yellow) and overbank (brown) deposits, representing sand and mud, respectively. Three timelines at t_1, t_2, and t_3 are shown. Blue lines trace channel trajectories; maximum channel depth defines the compensational depth (H_c). Figure modified from Esposito et al. (2018). (b) Identification of compensational timescale (T_c) from variability in the ratio of sedimentation to subsidence (σ_{ss}), calculated from windowed sedimentation rates (e.g., over Δt) relative to long-term subsidence rate. At $\Delta t/T_c = 1$, a break in regression slope is observed, from $\kappa_s < 1$ to $\kappa_l \approx 1$. (c) Schematics showing progressive reduction in σ_{ss} and eventual deterministic stacking of deposits, where sedimentation rate matches subsidence rate. Times t_1, t_2, and t_3 are arbitrary and used for illustration. Panels (b) and (c) are modified from Straub and Wang (2013).

the transition from spatially heterogeneous, autogenically dominated deposition to uniform basin filling (Wang et al., 2011; Hajek and Straub, 2017).

We computed σ_{ss} over window lengths from the highest temporal resolution of each dataset (1 h in physical and 50 yrs in numerical experiments) to half the total experiment duration. After log-transforming both σ_{ss} and T, we applied MATLAB change-point analysis (findchangepts, maximum three change points) and selected the first break point for which $\kappa_l > 0.8$. In all cases, at least one change point satisfied this criterion. Uncertainty was quantified by bootstrap resampling: spatial positions along the transect were resampled with replacement and the detection repeated 100 times per experiment; the interquartile range was reported as the uncertainty envelope.

2.3.3. *Computation of local and regional surface roughness*

We quantified topographic roughness at two scales: local roughness (H), which captures relief generated by individual channels, and regional roughness (D), which captures basin-scale departures from a smooth depositional profile.

Following previous studies (Wang et al., 2011; Trampush et al., 2017), we used maximum channel depth as the local topographic roughness metric. Channel depth at each time step was derived from cross-sectional topography using the Progressive Black Top Hat (PBTH) algorithm (Luo et al., 2015; Wang and Abels, 2025). PBTH iteratively applies grey-scale closing (dilation followed by erosion) using increasing window sizes to construct a local maximum surface; subtracting this surface from detrended topography isolates depressions and pixel-scale relief. Measurements represent channel or channel-belt dimensions for physical and numerical runs, respectively. For example, we applied a 7.0 cm moving window to the cross-section profile of TDB-20–1 at $t = 428.5$ h (see line location in Fig. 1a); the full workflow utilized windows of 3.5 to 10.5 cm. To suppress noise, we defined a depth threshold as the median PBTH value plus two median absolute deviations, with a minimum of 3 mm for physical experiments and 0.1 m for numerical experiments. Channels were defined as depressions between adjacent peaks that exceeded both thresholds, and the deepest channel per time step was recorded. Local roughness (H) was defined as the 95th percentile of these instantaneous maxima across all time steps. Visual inspection confirmed reliable channel identification (Fig. 3a).

Regional roughness measures how strongly the basin surface deviates from the graded profile expected under even sediment distribution (Straub and Wang, 2013). We defined the graded profile as the long-term mean topographic profile along the analysis transect, after removing the temporal vertical trend imposed by sea-level rise (Fig. 3c). Starting from raw cross-stream topography (Fig. 3b), we subtracted the trend from imposed sea-level rise rate ($r_{SL} = 0.25$ mm/h) and then removed the mean transect profile that captures basin-scale gradient from continuous inlet-fed sedimentation (Fig. 3c), yielding a residual elevation field (Fig. 3d). Negative residuals indicate unfilled space, whereas positive residuals indicate excess deposition (sensu Posamentier and Allen, 1999). We defined regional roughness (D) as the 95th percentile of the absolute residuals across space and time.

This approach follows the accommodation definition of Posamentier and Allen (1999): the space between the graded profile and the actual depositional surface. The graded profile used here provides an empirically grounded equilibrium surface, addressing the limitation noted by

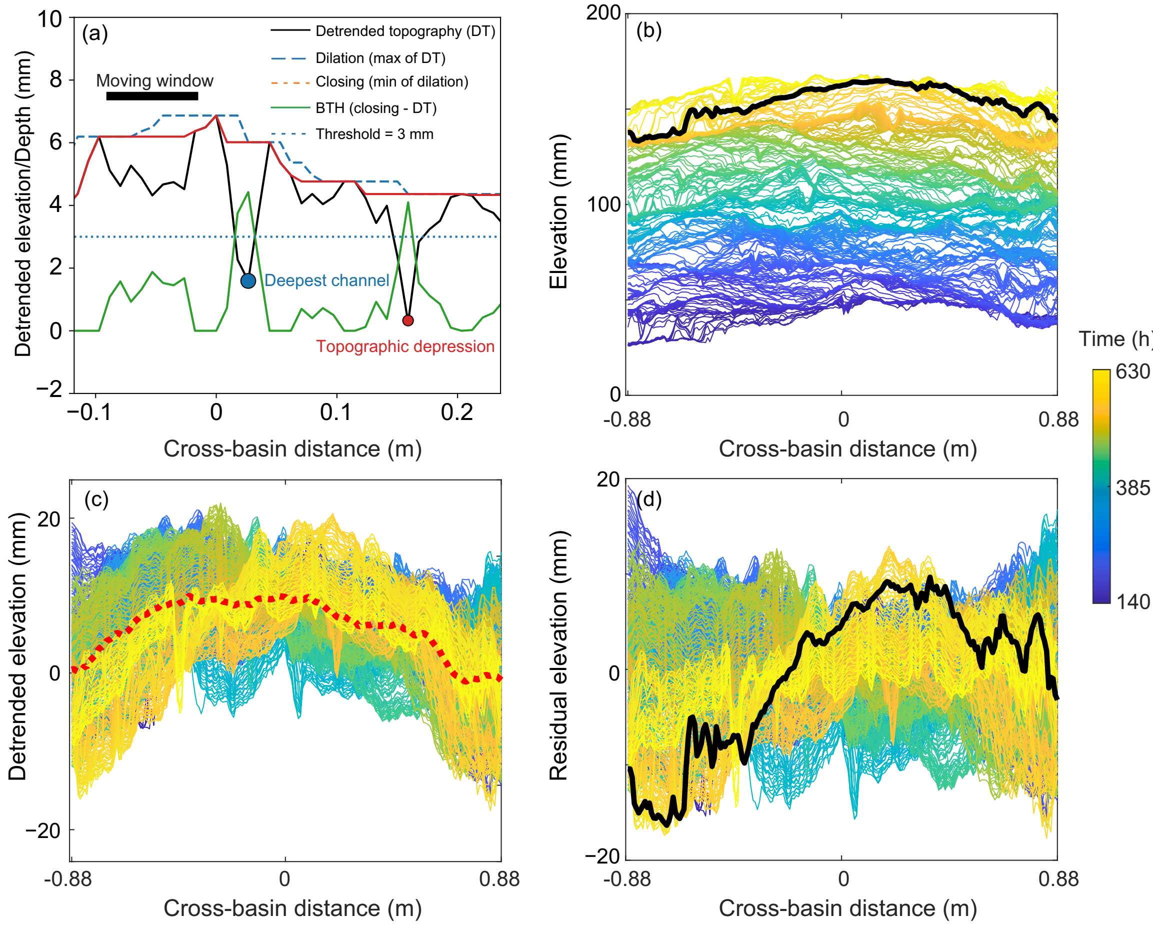

Fig. 3. Workflow for quantifying surface roughness. (a) Black top-hat (BTH) transformation applied to a detrended topographic profile from TDB-20–1 at $t = 428.5$ h. Detrended topography (black), dilated profile (blue dashed), closed profile (orange), BTH thickness (green), and channel depth threshold (horizontal blue line) are shown; detected depressions marked by red dots, with deepest channel highlighted. The BTH moving-window width applied is 7 cm. (b) Raw elevation profiles through time along the cross-stream transect (−88 cm to 88 cm; 0 at the basin axis; transect shown in Fig. 1a). (c) Time-detrended elevation profiles after removing background sea-level rise ($r_{SL} = 0.25$ mm/h); mean profile (red dashed line) shown. (d) Residual elevation profiles obtained by subtracting the mean profile in (c) from (b), yielding time- and space-detrended profiles; solid black lines in (b) and (d) mark the time step at which regional roughness (D) is reached.

Muto and Steel (2000) and Burgess et al. (2025) that such profiles are difficult to define from observations. Burgess et al. (2025) define accommodation more generally as mean potential deposition per unit time; while suited to forward modeling, our experiments satisfy this requirement through direct measurement of the graded profile.

In summary, H captures the depth of the deepest active channel at a given moment, while D captures the integrated spatial unevenness of the depositional surface relative to its long-term mean. Because D aggregates many spatial samples and time steps, individual channels exert limited influence; D is most sensitive to laterally extensive, persistent basin-scale asymmetry.

2.4. Dimensionless framework for cross-experiment comparison

We cast both the imposed forcing and the measured responses in dimensionless form to facilitate direct comparison between physical and numerical runs, which differ in dimensional scales (e.g., length, time, discharge) and boundary conditions. The control run provides the reference scales: a time scale T_{c0} (the compensational timescale under steady forcing), a length scale H_{c0} (the compensational depth corresponding to T_{c0}), and flux scales based on long-term mean water or sediment discharge (Q_{mean}).

Forcing is characterized by a dimensionless period $P^* = P/T_{c0}$; we refer to $P^* \langle 1$ as fast forcing and $P^* \rangle 1$ as slow forcing. We also define a dimensionless amplitude A^* that normalizes the forcing amplitude using its appropriate control scale. For Q_s/Q_w forcing, where sediment discharge varies at fixed water discharge, we define $A^* = A_Q/Q_{s,\ mean}$, with A_Q representing the amplitude of the $Q_s(t)$ oscillation, i.e., half the peak-to-trough range. With this definition, A^* spans 0.075–0.6 for physical runs and 0.05–0.4 for numerical runs.

Responses under cyclic forcing are scaled by their control values: $T_c^* = T_c'/T_{c0}$ for the compensation timescale, $H^* = H'/H_0$ for the local surface roughness, and $D^* = D'/D_0$ for regional surface roughness (where prime denotes the measured value of the metric in the experiment with varying external forcing, and subscript 0 indicates the same metric estimated from the control run).

2.5. Statistical analysis

To quantify the relationship between pairs of variables, we first evaluated the strength and direction of linear association using the Pearson correlation coefficient (r) and its corresponding p-value, testing the null hypothesis of no linear correlation. The coefficient r measures the degree of scatter around a linear relation (Weisberg, 2005); larger $|r|$ indicates stronger correlations, and $p < 0.05$ was taken as statistically significant. We then used linear regression to describe functional relationships between variables, with the coefficient of determination (R^2) representing the proportion of variance in the response explained by the predictor (Draper and Smith, 1998). Uncertainty in regression coefficients is reported as ±1 standard deviation from the least-square fit.

3. Results

3.1. Mass-extraction profiles and transect selection

The cumulative mass-extraction fraction χ increases monotonically with distance from the sediment source in both the physical and numerical experiments (Fig. 4a, b). The maximum retained fraction, χ_{max}, varies substantially among runs and is systematically higher in forced experiments than in unforced controls. In the physical experiments, the unforced control (TDB-12–1) retains the least sediment on the delta plain, with $\chi_{max} = 0.42$, meaning that 58% of the input mass bypasses the shoreline. The forced runs yield χ_{max} values ranging from 0.63 (TDB-16–3b) to 0.85 (TDB-20–1) (Fig. 4a, c–h). In the numerical experiments, retention is higher overall: the unforced control (NC) reaches $\chi_{max} = 0.86$, while forced runs range from 0.94 (A10P1.25) to 1.00 (A20P1.25, A20P10, A40P10) (Figs. 4b and S1).

We used these χ profiles to define the transect-selection window, $0.25\chi_{max} \le \chi \le 0.5\chi_{max}$ (Section 2.3.1). In the physical experiments,

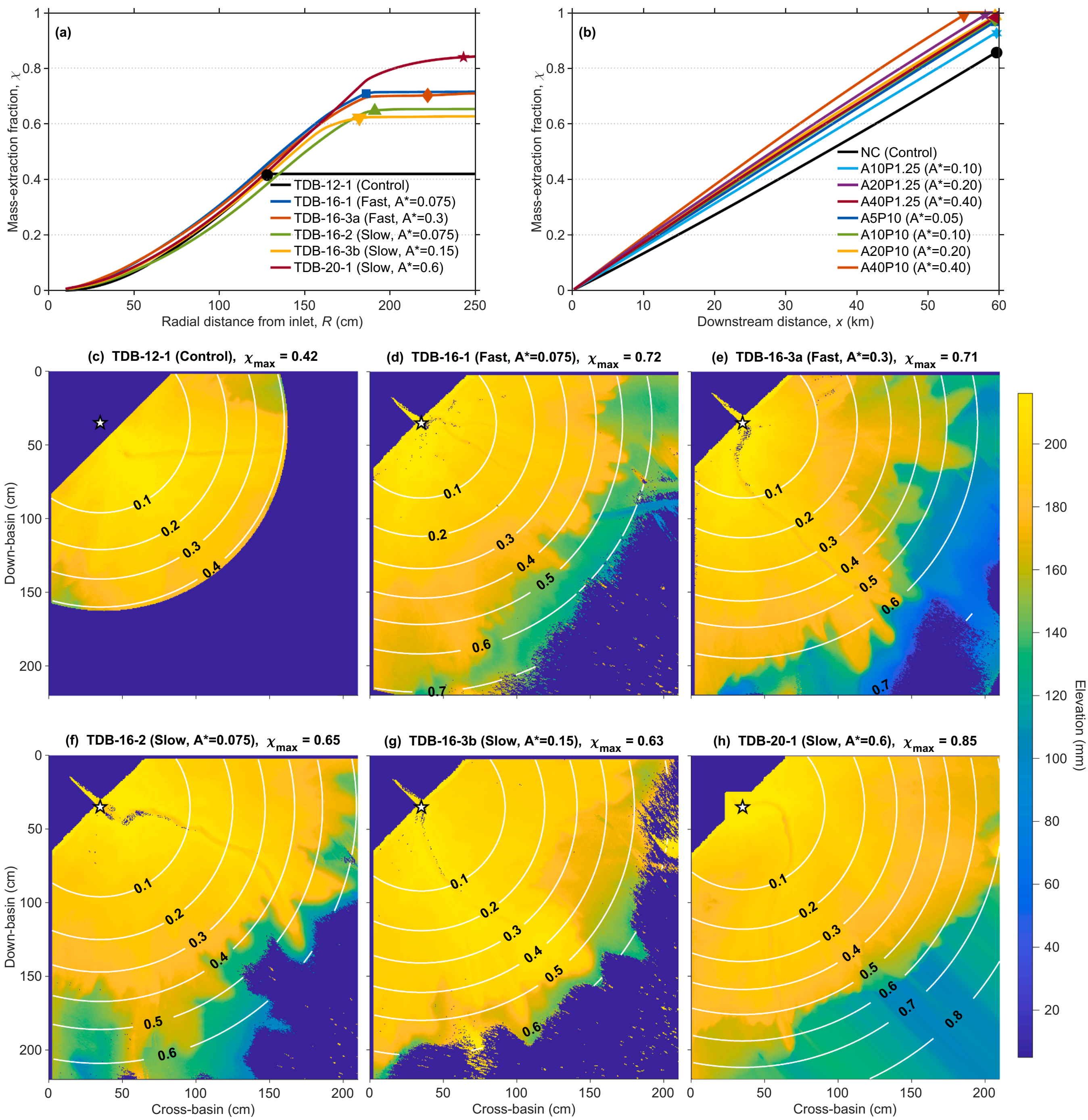

Fig. 4. Spatial distribution of the cumulative mass-extraction fraction χ. (a, b) χ as a function of distance from the sediment source for (a) the six physical experiments (radial distance R from the inlet) and (b) the eight numerical experiments (downstream distance x). Filled symbols mark χ_{max} for each experiment, defined as 99th percentile of the $\chi(R)$ or $\chi(x)$ distribution. (c)–(h) Final-timestep digital elevation models (DEMs) for TDB-12–1 (control), TDB-16–1, TDB-16–3a, TDB-16–2, TDB-16–3b, and TDB-20–1, respectively. Warm colors denote higher elevation. White contour lines show χ isopleths at intervals of 0.1, and white stars mark the inlet position.

transects were extracted at $\chi = 0.10$, 0.15, and 0.20, corresponding to radial distances of 51–86 cm from the apex. In the numerical experiments, transects were extracted at $\chi = 0.20$, 0.30, and 0.40, corresponding to downstream distances of 10.6–29.0 km from the upstream boundary.

3.2. Variations of compensation timescale within and across experiments

Before reporting T_c*, we verified that the long-term per-point sedimentation rate $\bar{r}(x)$ at each transect position agrees with the imposed sea-level rise rate in both physical (0.21–0.26 vs. 0.25 mm/hr; Figure S2) and numerical experiments (0.35–0.48 vs. 0.40 m/kyr; Figure S3).

Across all fourteen experiments and three χ positions per experiment, σ_{ss} displays well-defined slope breaks that identify T_c* (Figs. 5 and S4). Bootstrap interquartile ranges for T_c* are narrow, with a maximum width of 0.5 in the physical experiments and 0.4 in the numerical experiments. At timescales longer than T_c, κ_l ranges between 0.8 and 1.2, confirming compensational stacking. At shorter timescales, κ_s remains below the random-stacking threshold of 0.5 in most cases, indicating anti-compensational behavior.

Within the viable χ extraction window, T_c* is stable across measurement positions: the maximum spread across three χ values within any single experiment is 22% in the physical runs (TDB-20–1, T_c* = 2.3–2.8; Fig. 6a) and 19% in the numerical runs (A20P1.25, T_c* = 2.1–2.5; Fig. 6b). Given this stability, we adopt the middle extraction position ($\chi = 0.15$ for physical experiments, $\chi = 0.30$ for numerical experiments) as the representative transect for all inter-experiment comparisons; values at the flanking χ positions are provided in Figs. 5, 6, and S4.

T_c* varies systematically with A*, but the relationship is non-monotonic (Fig. 6). In the physical experiments at $\chi = 0.15$, the largest T_c* values occur at intermediate A*. Under fast forcing, TDB-16–1 yields T_c* = 3.7 [3.4–3.8] (parenthetic values denote 25th and 75th percentiles), far exceeding TDB-16–3a (T_c* = 1.0 [1.0, 1.1]). Under slow forcing, TDB-16–3b produces T_c* = 3.2 [3.0, 3.4], exceeding both the lower-amplitude TDB-16–2 (T_c* = 1.1 [1.1, 1.2]) and the higher-amplitude TDB-20–1 (T_c* = 2.4 [2.3, 2.6]) (Fig. 5). The numerical experiments at $\chi = 0.30$ reveal a parallel pattern. Among the fast-forcing

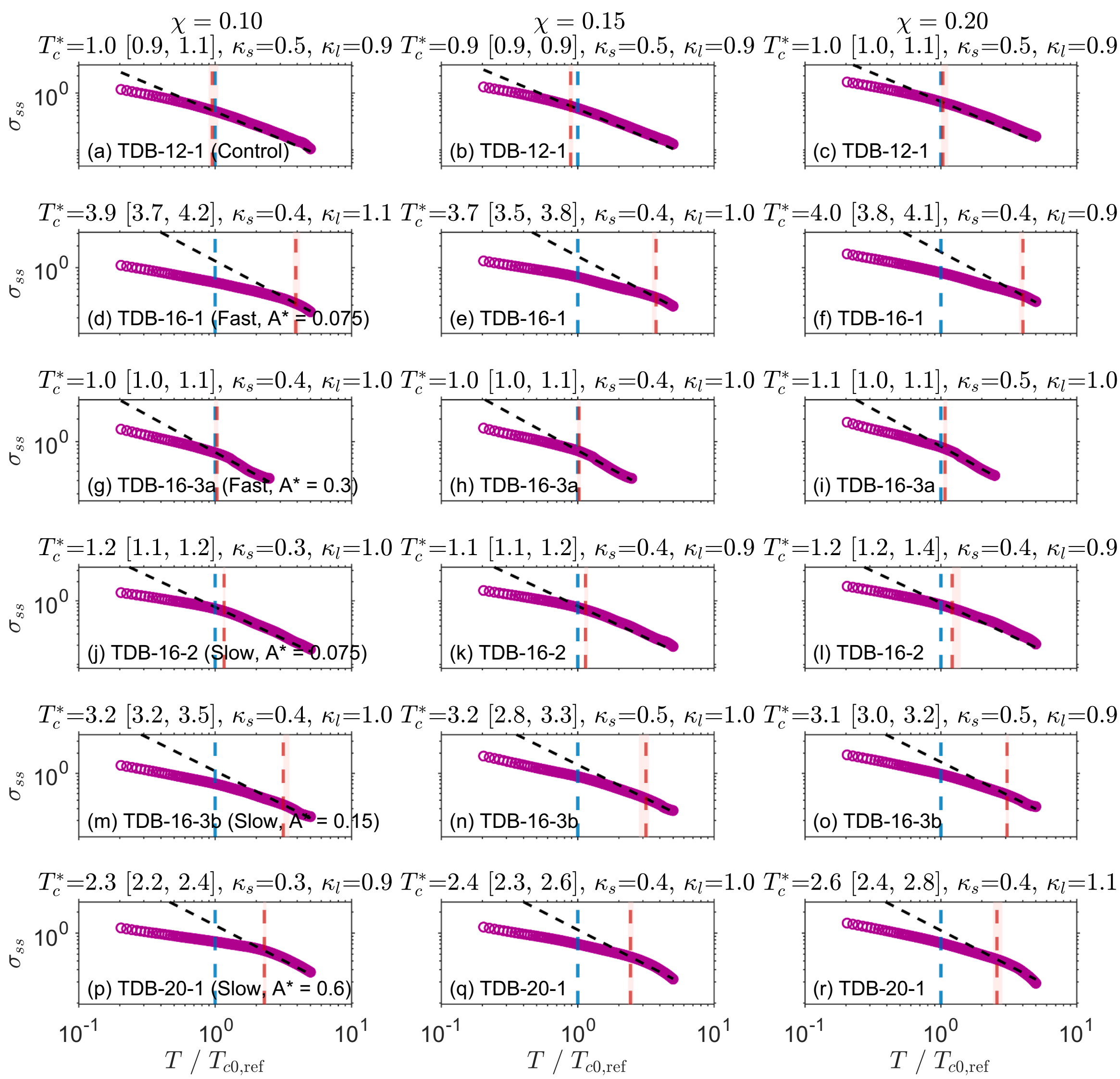

Fig. 5. The **variation of σ_{ss} as a function of normalized time-window length at multiple mass-extraction locations ($\chi = 0.10$, 0.15, and 0.20) for physical experiments.** Each row corresponds to one experiment (TDB-12–1 through TDB-20–1); columns correspond to $\chi = 0.10$, 0.15, and 0.20 from left to right. The x-axis is normalized by $T_{c0,ref} = 49$ h at $\chi = 0.10$ in TDB-12–1. Vertical blue and red dashed lines mark $T_{c0,ref}$ and the inferred T_c at the slope break, respectively. The dashed black line shows the $\kappa = 1$ power-law reference. Pink shading denotes the interquartile range of T_c* from bootstrap resampling ($n = 100$). Panel titles report T_c*, its interquartile range (in brackets), κ_s, and κ_l.

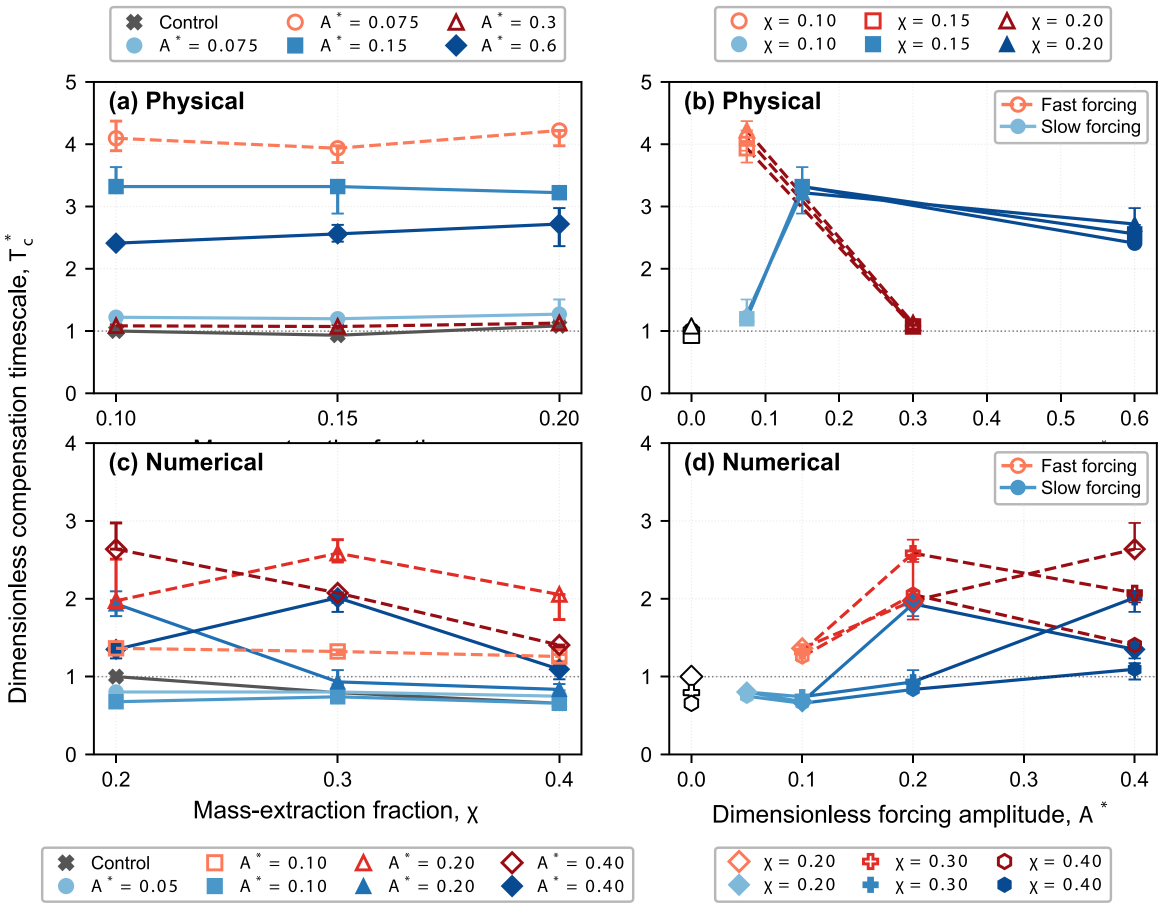

Fig. 6. Sensitivity of the dimensionless compensational timescale T_c* to mass-extraction fraction χ and dimensionless forcing amplitude A*. (a, c) T_c* as a function of χ for physical (a) and numerical (c) experiments; the horizontal dashed line marks $T_c{*} = 1$ (unforced baseline). (b, d) T_c* as a function of A* at the representative χ positions ($\chi = 0.10$, 0.15 and 0.20 for physical; $\chi = 0.20$, 0.30 and 0.40 for numerical). Fast-forcing and slow-forcing experiments are shown by filled and open symbols, respectively. Error bars denote the interquartile range of T_c* from bootstrap resampling ($n = 100$).

runs, A20P1.25 produces the highest $T_c{*} = 2.6$ [2.6, 3.0], exceeding both A10P1.25 ($T_c{*} = 1.3$ [1.3, 1.3]) and A40P1.25 ($T_c{*} = 2.1$ [2.0, 2.1]). Among the slow-forcing runs, T_c* increases more monotonically with A*: A40P10 reaches $T_c{*} = 2.0$ [1.9, 2.1], A20P10 yields $T_c{*} = 0.9$ [0.9, 1.0], and the two lowest-amplitude runs (A5P10, A10P10) remain below unity (Figs. 6 and S4).

3.3. *Variations of local and regional roughness within and across experiments*

Dimensionless local roughness H* and regional roughness D* quantify how forcing alters topographic variability relative to the unforced control, with $H{*} = D{*} = 1.0$ at the most proximal χ position in each control experiment (see Section 2.3.3 for definitions; Figs. 7 and S5).

Dimensionless local roughness, H*, is most sensitive to forcing amplitude. In the physical experiments, most forced runs produce H* near or below the control, which itself declines from 1.0 at $\chi = 0.10$ to 0.5 at $\chi = 0.20$ (Fig. 8a). The exceptions are two slow-forcing runs at the proximal position: TDB-16–2 ($H{*} = 1.4$) and TDB-16–3b ($H{*} = 1.5$), both of which decline downstream. TDB-20–1, the highest-amplitude slow run, yields the lowest H* among all forced experiments (0.5–0.8). Fast-forcing runs do not amplify local roughness relative to the control ($H{*} = 0.5$–1.0). Physical H* shows no clear monotonic relationship with A* (Fig. 8b). In numerical experiments, H* spans a wider range and increases nonlinearly with A*, with a pronounced jump above $A{*} = 0.20$ (Fig. 8c, d). The two highest-amplitude runs, A40P1.25 and A40P10, produce H* of 3.0–4.3. Scenario A20P1.25 reaches $H{*} = 2.7$ at the proximal position before declining to 1.8 downstream. All remaining numerical runs cluster near unity (0.9–1.4). Across both experiment suites, H* generally decreases downstream, with steeper attenuation under fast forcing.

Dimensionless regional roughness, D*, responds to both forcing amplitude and period. In the physical experiments, all forced runs produce $D{*} \geq 1.0$, and D* varies by <0.3 across the three χ positions within any given run (Fig. 8e). Among the slow-forcing runs, D* increases with A*, from TDB-16–2 ($D{*} = 1.3$–1.6) through TDB-16–3b (1.6–1.7) to TDB-20–1 (1.5–1.6). Under fast forcing, the relationship is non-monotonic: TDB-16–1 produces the highest D* of any physical run (1.8–2.0), while TDB-16–3a yields comparatively modest values (1.0–1.2) (Fig. 8f). In the numerical experiments, slow-forcing runs show a monotonic increase in D* with A*: A5P10 and A10P10 remain near or below unity, A20P10 reaches 0.9–1.2, and A40P10 stands above the rest at 1.7–2.1 (Fig. 8g, h). Fast-forcing runs produce systematically lower D* than their slow-forcing counterparts at equivalent A*: A40P1.25 reaches only 1.2–1.5, while A10P1.25 and A20P1.25 fall below unity. D* also decreases from proximal to distal positions in most numerical runs.

3.4. *Covariance between compensation timescale and roughness*

Regional roughness D* is a stronger predictor of T_c* than local roughness H* across all experiments and forcing regimes (Fig. 9). D* exhibits statistically significant positive correlations with T_c* under both fast forcing ($r = 0.81$, $p < 0.001$, $R^2 = 0.66$, $n = 15$) and slow forcing ($r = 0.89$, $p < 0.001$, $R^2 = 0.79$, $n = 21$), with regression slopes of 2.19 ± 0.44 and 2.47 ± 0.29, respectively, indicating that T_c* increases more

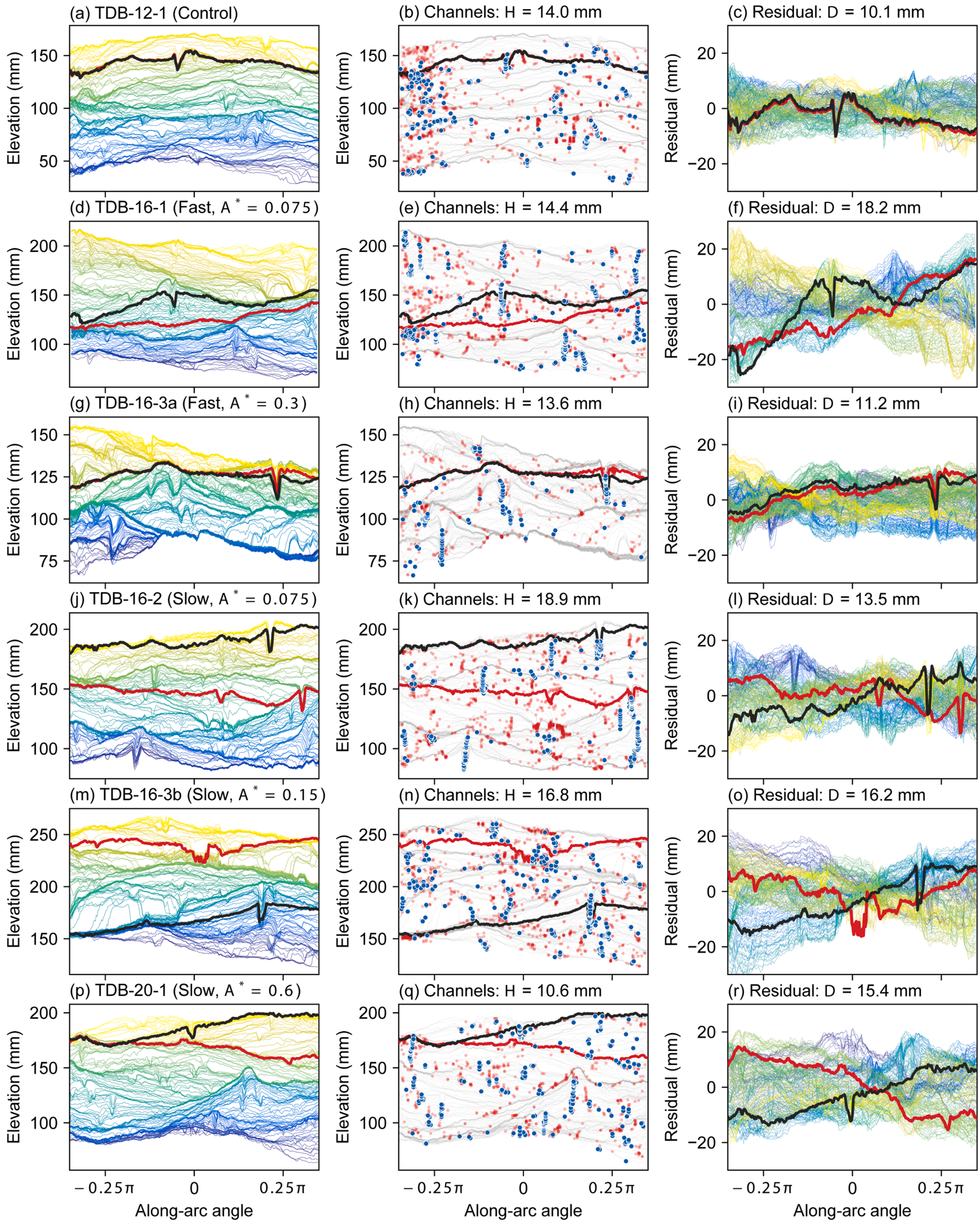

Fig. 7. Stratigraphic cross-sections extracted along transects at $\chi = 0.15$ for all physical experiments. Rows correspond to TDB-12–1 (control), TDB-16–1, TDB-16–3a, TDB-16–2, TDB-16–3b, and TDB-20–1 from top to bottom, in order of increasing forcing amplitude within each forcing regime (i.e., fast and slow). The three columns show, respectively: (left) the complete time sequence of elevation profiles; (center) the same profiles in grey with detected channel troughs overplotted as red dots and the deepest-channel location at each timestep as blue circles; (right) residual elevation after removing the experiment-mean spatial profile and the long-term aggradation trend. In all panels, the black profile marks the timestep corresponding to H, and the red profile marks the timestep corresponding to D.

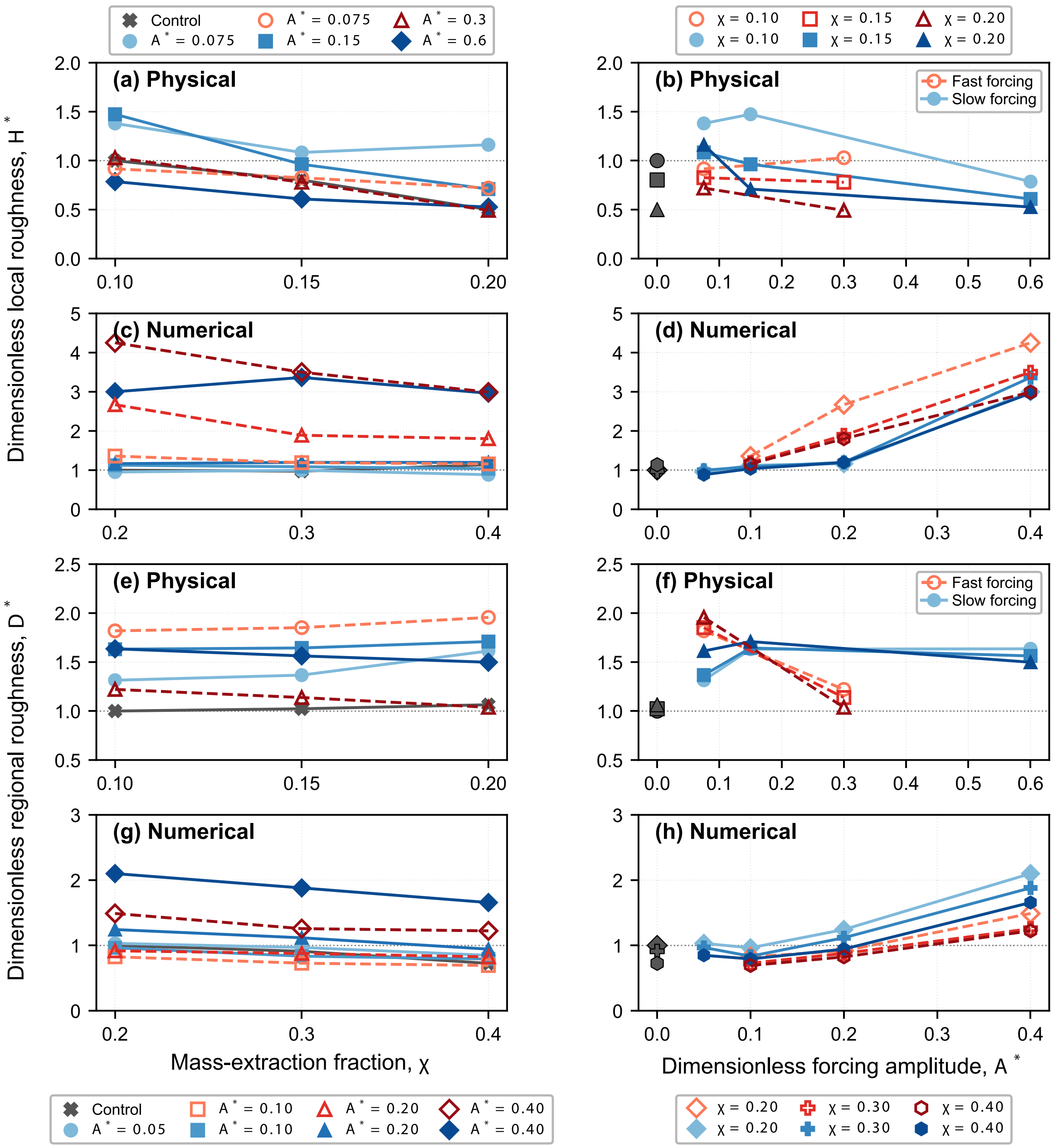

Fig. 8. Dimensionless local roughness (H^*) and regional roughness (D^*) as functions of mass-extraction fraction (χ, left column) and dimensionless forcing amplitude (A^*, right column). The upper two rows show H^* and the lower two rows show D^*, with physical experiments (a, b, e, f) and numerical experiments (c, d, g, h) alternating within each pair. The horizontal dashed line marks $H^* = D^* = 1.0$ (unforced baseline). Fast- and slow-forcing runs are distinguished by red dashed and blue solid lines, respectively. H^* is normalized by the control value at $\chi = 0.10$ (physical) or $\chi = 0.20$ (numerical); D^* is normalized at the same positions.

than proportionally with D^*. H^*, in contrast, yields weak and statistically insignificant correlations with T_c^* under both fast forcing ($r = -0.05$, $p = 0.85$, $n = 15$) and slow forcing ($r = 0.36$, $p = 0.11$, $n = 21$).

4. Discussion

4.1. Cyclic forcing extends the compensation timescale by enhancing regional roughness

In both physical and numerical experiments, cyclic forcing systematically lengthens the compensation timescale by generating basin-scale topographic relief. The strong positive correlation between D^* and T_c^* ($r = 0.81$–0.89; Fig. 9), coupled with the absence of a significant correlation between H^* and T_c^*, indicates that regional roughness, not local channel depth, is the primary control on compensational dynamics. D^* integrates the cumulative effect of channel-belt positioning, lobe switching, and differential aggradation across the transect; H^*, by contrast, captures only the depth of the deepest active channel at a given time. The compensation timescale reflects the time required for the depositional system to visit and fill spatially distributed topographic lows across the basin (Straub et al., 2009); D^* is a direct measure of that distributed relief, which explains its predictive power over H^*.

The mechanism linking cyclic forcing to elevated D^* operates through asymmetric sediment routing. Oscillations in sediment-to-water discharge ratio confine channels during low-supply phases and concentrate deposition in active lobes during high-supply phases, producing persistent topographic highs and lows that accumulate over multiple forcing cycles (Figs. 7 and S5). Adjacent areas remain sediment-starved, enhancing surface roughness and prolonging channel residence time. This behavior is consistent with experimental and numerical

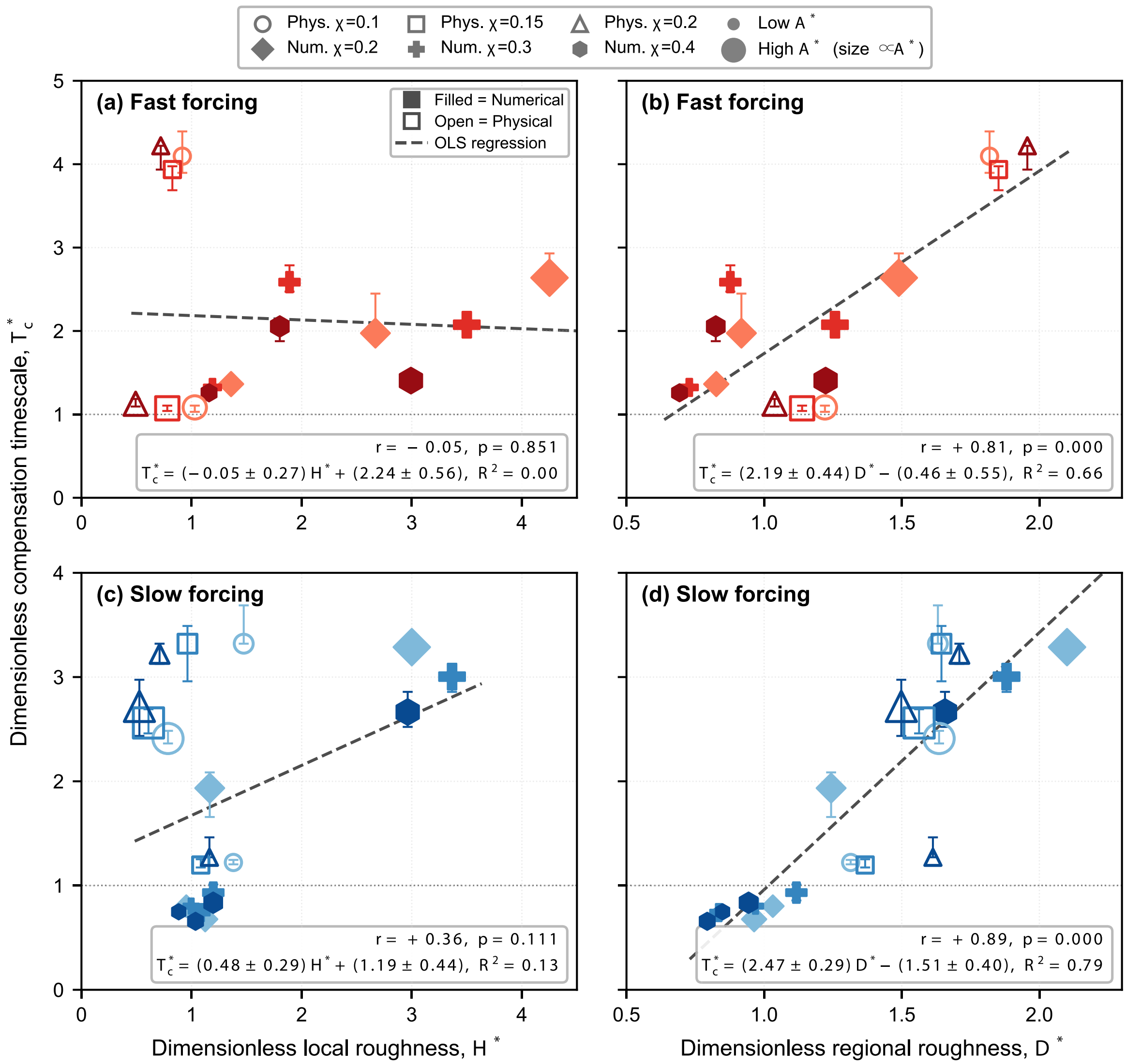

Fig. 9. Covariance between dimensionless compensation timescale (T_c*) and dimensionless roughness metrics (local, H*; regional, D*) across combined numerical and physical experiments, separated by **forcing** regimes. (a) T_c* versus H* for fast forcing. (b) T_c* versus D* for fast forcing. (c) T_c* versus H* for slow forcing. (d) T_c* versus D* for slow forcing. Vertical error bars span the interquartile range (25th–75th percentile) of T_c* across transect positions within each experiment. The dashed black line in each panel shows the ordinary least-squares (OLS) regression.

studies showing that cyclic sediment supply delays deterministic sedimentation dynamics by sustaining lateral gradients in aggradation rate (Wang et al., 2021), and with observations that reduced sediment supply promotes channel incision and topographic locking in alluvial systems (Kim and Paola, 2007; Sun et al., 2002; Whipple et al., 1998). The anti-compensational basin-filling behavior implied by $\kappa_s < 0.5$ across most forced experiments (Figs. 5 and S4) further supports this interpretation. As A* increases, a larger fraction of sediment is retained in the proximal zone (Fig. 4), consistent with reduced lateral channel switching rates predicted by previous models (Edmonds and Slingerland, 2010). Although avulsion frequency was not directly quantified, spatially locked channels, sustained basin-scale asymmetry in topography (Figs. 7 and S5), and enhanced sediment retention (Fig. 4) imply delayed attainment of avulsion thresholds (Mohrig et al., 2000; Slingerland and Smith, 2004).

These results speak to a longstanding question about whether autogenic dynamics act as a low-pass filter that shreds externally imposed signals before preservation (Jerolmack and Paola, 2010; Griffin et al., 2023; Romans et al., 2016). Alternative frameworks emphasize that sediment-routing systems can transfer and even amplify climatic signals under certain conditions (Armitage et al., 2011; Castelltort and Van Den Driessche, 2003; Simpson and Castelltort, 2012). Our findings suggest a more nuanced picture: a forcing signal does not simply pass through or get destroyed by autogenic dynamics, but instead reorganizes them, locking channels in place and elevating regional roughness. The resulting extension of T_c implies that the autogenic 'shredding' threshold is not fixed but shifts in response to the forcing itself. This coupling between allogenic and autogenic processes complicates the signal-to-noise framing (Romans et al., 2016; Straub et al., 2020). Forward modeling of submarine fans has shown that autogenic dynamics alone can produce ordered strata with statistically significant bed-thickness trends, making allogenic signals difficult to isolate even when present (Burgess et al., 2019; Burgess and Duller, 2024). Our results extend this insight to fluvio-deltaic systems: the 'noise' floor is not merely difficult to separate from the 'signal' but is itself a function of it.

4.2. Implications for signal preservation in the stratigraphic record

The compensation timescale sets a fundamental limit on the temporal resolution of information preserved in stratigraphy: external signals with periods longer than T_c are more likely to be preserved, while shorter-period signals require higher amplitudes to be recorded

(Foreman and Straub, 2017; Toby et al., 2019a, 2022). This threshold is one component of the broader timescale hierarchy that links sediment production, transfer, and burial across a range of response times (Allen, 2008; Duller et al., 2019). Previous studies have largely characterized this threshold under steady or slowly varying conditions, with limited attention to how cyclic forcing modifies T_c itself (Wang et al., 2021; Toby et al., 2022). Our results refine this framework in two ways.

First, because forcing modifies T_c, the preservation threshold co-evolves with the forcing rather than remaining fixed. Under slow, high-amplitude forcing, T_c* increases by a factor of 2–4 (Fig. 6), extending the time required for sedimentation patterns to converge with the long-term aggradation rate. This creates a trade-off absent from the steady-state theory: the same forcing that generates the most conspicuous architectural response (e.g., basin-scale asymmetry in topography) also lengthens the compensational timescale, thereby coarsening the temporal resolution of the stratigraphic archive. Such systems can faithfully record only longer-duration signals. The boundary between faithful recording and signal loss is therefore not sharp; the extension of T_c is itself a depositional response to the forcing, so that the environmental signal simultaneously modifies the resolution of the archive that records it. If forcing intensity varies over geologic time—as during orbital cycles—T_c adjusts accordingly, meaning that the temporal resolution of the archive is not a fixed property of the depositional system but a function of its forcing history.

Second, at 2-D and 3-D scales, high-amplitude slow forcing produces directly visible architectural patterns: persistent topographic highs, asymmetric aggradation, and laterally restricted channels (Figs. 7 and S5). At the 1-D scale, however, longer T_c* lengthens the time and thickness required for a vertical section to record compensational stacking. Stratigraphic incompleteness—the absence of deposition at any single location during intervals when the channel is active elsewhere—means that individual vertical sections contain temporal gaps at timescales below T_c (Sadler, 1981; Straub et al., 2020). Extended T_c under forcing therefore increases the likelihood of such gaps in 1-D records, and forcing signals may go unrecognized in vertical sections even where 2-D and 3-D stratigraphic architecture is visibly organized. Multi-dimensional approaches, such as correlated outcrop panels, seismic cross-sections, or composite multi-well sections (Huang et al., 2025; Straub and Foreman, 2018; Sylvester, 2023; Zhang et al., 2022), sample multiple lateral positions simultaneously and are likely better suited to detect forcing signals. More broadly, our results indicate that interpreting the temporal resolution of ancient fluvio-deltaic strata requires accounting not only for what signals were imposed on the system, but for how those signals reshaped the system's capacity to record them.

Several limitations of this study warrant mention. First, all forced experiments imposed cyclic variations in the sediment-to-water discharge ratio; forcing through base-level change was not explored. Base-level forcing modulates accommodation creation rather than sediment supply directly and stratigraphic responses can be sensitive to the phasing between accommodation creation and sediment supply (Jervey, 1988; Muto and Steel, 1997; Posamentier and Allen, 1999), so the T_c response to base-level forcing remains to be tested. Second, the physical experiments used a cohesive sediment mixture that stabilizes channel banks and promotes channelized flow (Edmonds and Slingerland, 2010; Hoyal and Sheets, 2009). Non-cohesive systems, including pre-vegetation fluvial landscapes on early Earth and Mars (Gibling and Davies, 2012), may exhibit greater lateral channel mobility (Ielpi and Lapôtre, 2020; Li et al., 2026), potentially altering compensational behavior under forcing. Third, all analyses are based on 2-D cross-stream transects extracted at fixed mass-extraction fractions. Full 3-D lobe switching and radial sediment dispersal, both characteristic of natural fan-delta (Ganti et al., 2014), are not resolved by this approach, and whether the T_c extension documented here persists when 3-D avulsion and lobe-building cycles are explicitly tracked remains an open question. These limitations suggest that while the co-evolution of T_c with forcing is likely a general feature of depositional systems, the quantitative scaling relationships reported here should be tested across a broader range of forcing mechanisms, sediment properties, and spatial dimensions.

5. Conclusions

Using paired physical and numerical experiments, we show that cyclic water-sediment forcing systematically modifies the compensation timescale and topographic character of fluvio-deltaic depositional systems. Three principal findings emerge:

(1) Cyclic forcing extends the compensation timescale relative to unforced controls, with T_c* increasing by a factor of 2–4 under moderate-to-high amplitude forcing. The relationship between T_c* and forcing amplitude is non-monotonic under fast forcing: intermediate amplitudes produce the longest compensation timescales, while both weak and strong forcing yield values closer to the unforced baseline. Under slow forcing, T_c* increases more monotonically with amplitude, though the weakest runs fail to extend T_c* beyond the control.

(2) Regional topographic roughness (D*), not local channel depth (H*), is the primary predictor of compensation timescale. D* correlates strongly with T_c* under both fast and slow forcing (r = 0.81–0.89, $p < 0.001$), whereas H* shows no statistically significant correlation. Slow forcing produces systematically higher D* than fast forcing at equivalent amplitude, and this period dependence is mirrored in T_c*.

(3) Because forcing itself modifies T_c, the temporal resolution of the stratigraphic archive co-evolves with the environmental conditions being recorded. High-amplitude slow forcing generates the most conspicuous depositional architecture but simultaneously coarsens the archive by increasing stratigraphic incompleteness at individual vertical sections. Multi-dimensional observational approaches, including correlated outcrop panels, seismic cross-sections, and composite well sections, are therefore better suited than single 1-D sections for detecting forcing signals in ancient fluvio-deltaic strata.

Together, these results demonstrate that the stratigraphic record is not a passive filter with a fixed temporal resolution. Its fidelity depends on the amplitude and period of the forcing it experienced, with regional topographic roughness serving as the mechanistic link between forcing regime and preservation threshold.

Data availability

All data needed to evaluate the conclusions in the paper are present in the paper and/or the Supplementary Materials. Original datasets of numerical experiments are available at Wang et al. (2020) and Wang (2025), while those of laboratory experiments are available at Li and Straub (2020), Toby and Straub (2019a, 2019b), Toby et al. (2019b), and Straub (2025). Postprocessed data and code to generate the results of this study will be made publicly available upon acceptance at Zenodo via https://doi.org/10.5281/zenodo.14872658.

CRediT authorship contribution statement

Youwei Wang: Writing – review & editing, Writing – original draft, Visualization, Validation, Software, Methodology, Investigation, Formal analysis, Data curation, Conceptualization. **Vamsi Ganti:** Writing – review & editing, Writing – original draft, Validation, Supervision, Project administration, Methodology, Investigation, Funding acquisition, Formal analysis. **Ajay B. Limaye:** Writing – review & editing, Writing – original draft, Validation, Supervision, Project administration, Methodology, Investigation, Funding acquisition, Formal analysis. **Kyle M. Straub:** Writing – review & editing, Writing – original draft, Visualization, Validation, Supervision, Software, Resources, Project administration, Methodology, Investigation, Funding acquisition, Formal analysis, Data curation, Conceptualization.

Declaration of competing interest

The authors declare that they have no known competing financial interests or personal relationships that could have appeared to influence the work reported in this paper.

Acknowledgments

This work was sponsored by the Second Tibetan Plateau Scientific Expedition and Research (STEP) program (2024QZKK0301) that supports Y.W., the National Science Foundation (EAR2310740) grant to V. G. that supports Y.W. and V.G., the American Chemical Society Petroleum Research Fund (ACS PRF 65852-DNI8) to A.B.L. that supports Y.W. and A.B.L., and the National Science Foundation (grant EAR-1424312) to K.M.S. We thank Chris Paola for inspiring discussions, Editor Jean-Philippe Avouac, Peter Burgess and one anonymous reviewer for constructive comments that helped improve an earlier version of this manuscript.

Supplementary materials

Supplementary material associated with this article can be found, in the online version, at doi:10.1016/j.epsl.2026.120177.

References

Abels, H.A., Clyde, W.C., Gingerich, P.D., Hilgen, F.J., Fricke, H.C., Bowen, G.J., Lourens, L.J., 2012. Terrestrial carbon isotope excursions and biotic change during palaeogene hyperthermals. Nat. Geosci. 5, 326–329. https://doi.org/10.1038/ngeo1427.

Allen, P.A., 2008. From landscapes into geological history. Nature 451, 274–276. https://doi.org/10.1038/nature06586.

Armitage, J.J., Duller, R.A., Whittaker, A.C., Allen, P.A., 2011. Transformation of tectonic and climatic signals from source to sedimentary archive. Nat. Geosci. 4, 231–235. https://doi.org/10.1038/ngeo1087.

Bernhardt, A., Schwanghart, W., Hebbeln, D., Stuut, J.-B.W., Strecker, M.R., 2017. Immediate propagation of deglacial environmental change to deep-marine turbidite systems along the Chile convergent margin. Earth Planet. Sci. Lett. 473, 190–204. https://doi.org/10.1016/j.epsl.2017.05.017.

Blum, M.D., Törnqvist, T.E., 2000. Fluvial responses to climate and sea-level change: a review and look forward. Sedimentology 47, 2–48. https://doi.org/10.1046/j.1365-3091.2000.00008.x.

Burgess, P.M., Duller, R.A., 2024. Autogenic masking of allogenic inputs: numerical modelling of signal preservation in deep-water fan strata. Earth Planet. Sci. Lett. 628, 118583. https://doi.org/10.1016/j.epsl.2024.118583.

Burgess, P.M., Masiero, I., Toby, S.C., Duller, R.A., 2019. A big fan of signals? Exploring autogenic and allogenic process and product In a numerical stratigraphic forward model of submarine-fan development. J. Sediment. Res. 89, 1–12. https://doi.org/10.2110/jsr.2019.3.

Burgess, P.M., Prather, B.E., Steel, R., Falivene, O., 2025. A quantitative definition of accommodation: implications for understanding and prediction of strata. Sci. Adv. 11, 41. https://doi.org/10.1126/sciadv.ady7895.

Castelltort, S., Van Den Driessche, J., 2003. How plausible are high-frequency sediment supply-driven cycles in the stratigraphic record? Sediment. Geol. 157, 3–13. https://doi.org/10.1016/S0037-0738(03)00066-6.

Dong, T.Y., Nittrouer, J.A., Carlson, B., McElroy, B., Il'icheva, E., Pavlov, M., Ma, H., 2023. Impacts of tectonic subsidence on basin depth and Delta lobe building. J. Geophys. Res.: Earth Surf. 128, e2022JF006819. https://doi.org/10.1029/2022JF006819.

Draper, N.R., Smith, H., 1998. Regression in matrix terms: straight line case. Applied Regression Analysis. John Wiley & Sons, Ltd, pp. 115–134. https://doi.org/10.1002/9781118625590.ch4.

Duller, R.A., Armitage, J.J., Manners, H.R., Grimes, S., Jones, T.D., 2019. Delayed sedimentary response to abrupt climate change at the paleocene-eocene boundary, northern Spain. Geology. 47, 159–162. https://doi.org/10.1130/G45631.1.

Edmonds, D.A., Slingerland, R.L., 2010. Significant effect of sediment cohesion on delta morphology. Nat. Geosci. 3, 105–109. https://doi.org/10.1038/ngeo730.

Esposito, C.R., Di Leonardo, D., Harlan, M., Straub, K.M., 2018. Sediment storage partitioning in alluvial stratigraphy: the influence of discharge variability. J. Sediment. Res. 88, 717–726. https://doi.org/10.2110/jsr.2018.36.

Foreman, B.Z., Straub, K.M., 2017. Autogenic geomorphic processes determine the resolution and fidelity of terrestrial paleoclimate records. Sci. Adv. 3, e1700683. https://doi.org/10.1126/sciadv.1700683.

Ganti, V., Chu, Z., Lamb, M.P., Nittrouer, J.A., Parker, G., 2014. Testing morphodynamic controls on the location and frequency of river avulsions on fans versus deltas: huanghe (Yellow River), China. Geophys. Res. Lett. 41, 7882–7890. https://doi.org/10.1002/2014GL061918.

Gibling, M.R., Davies, N.S., 2012. Palaeozoic landscapes shaped by plant evolution. Nat. Geosci 5, 99–105. https://doi.org/10.1038/ngeo1376.

Griffin, C., Duller, R.A., Straub, K.M., 2023. The degradation and detection of environmental signals in sediment transport systems. Sci. Adv. 9, eadi8046. https://doi.org/10.1126/sciadv.adi8046.

Hajek, E.A., Straub, K.M., 2017. Autogenic sedimentation in clastic stratigraphy. Annu Rev. Earth. Planet. Sci. 45, 681–709. https://doi.org/10.1146/annurev-earth-063016-015935.

Hajek, E.A., Wolinsky, M.A., 2012. Simplified process modeling of river avulsion and alluvial architecture: connecting models and field data. Sediment. Geol. 257-260, 1–30. https://doi.org/10.1016/j.sedgeo.2011.09.005.

Hoyal, D.C.J.D., Sheets, B.A., 2009. Morphodynamic evolution of experimental cohesive deltas. J. Geophys. Res.: Earth Surf. 114. https://doi.org/10.1029/2007JF000882.

Huang, R., Li, M., Qiu, R., Wang, Y., Zhang, R., Jin, Z., 2025. Enhancing astronomical signal detection in cyclostratigraphy by superimposed averaging of paleoclimate proxies. Paleoceanogr. Paleoclimatol. 40, e2025PA005135. https://doi.org/10.1029/2025PA005135.

Ielpi, A., Lapôtre, M.G.A., 2020. A tenfold slowdown in river meander migration driven by plant life. Nat. Geosci. 13, 82–86. https://doi.org/10.1038/s41561-019-0491-7.

Jerolmack, D.J., Paola, C., 2010. Shredding of environmental signals by sediment transport. Geophys. Res. Lett. 37. https://doi.org/10.1029/2010GL044638.

Jerolmack, D.J., Sadler, P., 2007. Transience and persistence in the depositional record of continental margins. J. Geophys. Res.: Earth Surf. 112. https://doi.org/10.1029/2006JF000555.

Jervey, M.T., 1988. Quantitative geological modeling of siliciclastic rock sequences and their seismic expression. In: Wilgus, C.K., Hastings, B.S., Posamentier, H., Wagoner, J.V., Ross, C.A., Kendall, C.G.St.C. (Eds.), Sea-Level Changes: An Integrated Approach. Society of Economic Paleontologists and Mineralogists, p. 0. https://doi.org/10.2110/pec.88.01.0047.

Karssenberg, D., Bridge, J.S., 2008. A three-dimensional numerical model of sediment transport, erosion and deposition within a network of channel belts, floodplain and hill slope: extrinsic and intrinsic controls on floodplain dynamics and alluvial architecture. Sedimentology 55, 1717–1745. https://doi.org/10.1111/j.1365-3091.2008.00965.x.

Kim, W., Paola, C., 2007. Long-period cyclic sedimentation with constant tectonic forcing in an experimental relay ramp. Geology. 35, 331. https://doi.org/10.1130/G23194A.1.

Li, J., Parker, G., Wang, Y., Basheer, A., 2026. Width-dependent acceleration of meander migration in unvegetated rivers. Earth Planet. Sci. Lett. 681, 119939. https://doi.org/10.1016/j.epsl.2026.119939.

Li, Q., Straub, K.M., 2020. TDB_12_1. 10.5967/M03N21GX.

Luo, W., Pingel, T., Heo, J., Howard, A., Jung, J., 2015. A progressive black top hat transformation algorithm for estimating valley volumes on Mars. Comput. Geosci. 75, 17–23. https://doi.org/10.1016/j.cageo.2014.11.003.

McLain, M.C., Santi, P.M., Pyles, D.R., 2024. Debris-flow avulsion tendency estimated from boreholes or channel cuts. Geomorphology 455, 109190. https://doi.org/10.1016/j.geomorph.2024.109190.

Mohrig, D., Heller, P.L., Paola, C., Lyons, W.J., 2000. Interpreting avulsion process from ancient alluvial sequences: guadalope-Matarranya system (northern Spain) and Wasatch Formation (western Colorado). Geol. Soc. Am. Bull. 17.

Muto, T., Steel, R., 2000. The accommodation concept in sequence stratigraphy: some dimensional problems and possible redefinition. Sediment. Geol. 130, 1–10. https://doi.org/10.1016/S0037-0738(99)00107-4.

Muto, T., Steel, R., 1997. Principles of regression and transgression: the nature of the interplay between accommodation and sediment supply. J. Sediment. Res. 67, 994–1000. https://doi.org/10.1306/D42686A8-2B26-11D7-8648000102C1865D.

Paola, C., Martin, J.M., 2012. Mass-balance effects In depositional systems. J. Sediment. Res. 82, 435–450. https://doi.org/10.2110/jsr.2012.38.

Pederson, C.A., Santi, P.M., Pyles, D.R., 2015. Relating the compensational stacking of debris-flow fans to characteristics of their underlying stratigraphy: implications for geologic hazard assessment and mitigation. Geomorphology 248, 47–56. https://doi.org/10.1016/j.geomorph.2015.06.030.

Posamentier, H., Allen, G., 1999. Siliciclastic sequence stratigraphy: concepts and applications, v7. Concepts in sedimentology and paleontology.

Romans, B.W., Castelltort, S., Covault, J.A., Fildani, A., Walsh, J.P., 2016. Environmental signal propagation in sedimentary systems across timescales. Earth-Sci. Rev. 153, 7–29. https://doi.org/10.1016/j.earscirev.2015.07.012.

Sadler, P.M., 1981. Sediment accumulation rates and the completeness of stratigraphic sections. J. Geol. 89 (5), 569–584.

Sheets, B.A., Hickson, T.A., Paola, C., 2002. Assembling the stratigraphic record: depositional patterns and time-scales in an experimental alluvial basin. Basin Res. 14, 287–301. https://doi.org/10.1046/j.1365-2117.2002.00185.x.

Simpson, G., Castelltort, S., 2012. Model shows that rivers transmit high-frequency climate cycles to the sedimentary record. Geology. 40, 1131–1134. https://doi.org/10.1130/G33451.1.

Slingerland, R., Smith, N., 2004. River avulsions and deposits. Annu Rev. Earth. Planet. Sci. 32, 257–285. https://doi.org/10.1146/annurev.earth.32.101802.120201.

Straub, K., 2025. Data for analyzing compensational timescale in an experiment driven by high-amplitude, long-period sediment supply forcing at the Tulane Delta Basin (TDB-20-1). https://doi.org/10.5281/zenodo.17043341.

Straub, K.M., Duller, R.A., Foreman, B.Z., Hajek, E.A., 2020. Buffered, incomplete, and shredded: the challenges of reading an imperfect stratigraphic record. J. Geophys. Res.: Earth Surf. 125, e2019JF005079. https://doi.org/10.1029/2019JF005079.

Straub, K.M., Foreman, B.Z., 2018. Geomorphic stasis and spatiotemporal scales of stratigraphic completeness. Geology. 46, 311–314. https://doi.org/10.1130/G40045.1.

Straub, K.M., Li, Q., Benson, W.M., 2015. Influence of sediment cohesion on deltaic shoreline dynamics and bulk sediment retention: a laboratory study. Geophys. Res. Lett. 42, 9808–9815. https://doi.org/10.1002/2015GL066131.

Straub, K.M., Paola, C., Mohrig, D., Wolinsky, M., George, T., 2009. Compensational stacking of channelized sedimentary deposits. J. Sediment. Res. 79, 673–688. https://doi.org/10.2110/jsr.2009.070.

Straub, K.M., Wang, Y., 2013. Influence of water and sediment supply on the long-term evolution of alluvial fans and deltas: statistical characterization of basin-filling sedimentation patterns. J. Geophys. Res.: Earth Surf. 118, 1602–1616. https://doi.org/10.1002/jgrf.20095.

Strong, N., Paola, C., 2010. Valleys that never were: time surfaces versus stratigraphic surfaces. J. Sediment. Res. 80, 4–5. https://doi.org/10.2110/jsr.2010.007.

Sun, T., Paola, C., Parker, G., Meakin, P., 2002. Fluvial fan deltas: linking channel processes with large-scale morphodynamics. Water. Resour. Res. 38. https://doi.org/10.1029/2001WR000284, 26-1-26–10.

Sylvester, Z., 2023. Automated multi-well stratigraphic correlation and model building using relative geologic time. Basin Res. 35, 1961–1984. https://doi.org/10.1111/bre.12787.

Tasistro-Hart, A.R., Macdonald, F.A., Crowley, J.L., Schmitz, M.D., 2025. Four-million-year Marinoan snowball shows multiple routes to deglaciation. Proc. Natl. Acad. Sci. U.S.A. 122, e2418281122. https://doi.org/10.1073/pnas.2418281122.

Toby, S.C., Duller, R.A., De Angelis, S., Straub, K.M., 2022. Morphodynamic limits to environmental signal propagation across landscapes and into strata. Nat. Commun. 13, 292. https://doi.org/10.1038/s41467-021-27776-6.

Toby, S.C., Duller, R.A., De Angelis, S., Straub, K.M., 2019a. A stratigraphic framework for the preservation and shredding of environmental signals. Geophys. Res. Lett. 46, 5837–5845. https://doi.org/10.1029/2019GL082555.

Toby, S.C., Dutt, R., Akintomide, A., Straub, K.M., 2019b TDB_16_3 [WWW Document]. https://doi.org/10.26009/s0c20606.

Toby, S.C., Straub, K., 2019a. TDB_16_1 [WWW Document]. https://doi.org/10.26009/s0iorjdx.

Toby, S.C., Straub, K.M., 2019b TDB_16_2 [WWW Document]. https://doi.org/10.26009/s0xtyi86.

Tofelde, S., Bernhardt, A., Guerit, L., Romans, B.W., 2021. Times associated with source-to-sink propagation of environmental signals during landscape transience. Front. Earth Sci. 9, 628315. https://doi.org/10.3389/feart.2021.628315.

Trampush, S.M., Hajek, E.A., Straub, K.M., Chamberlin, E.P., 2017. Identifying autogenic sedimentation in fluvial-deltaic stratigraphy: evaluating the effect of outcrop-quality data on the compensation statistic. J. Geophys. Res.: Earth Surf. 122, 91–113. https://doi.org/10.1002/2016JF004067.

Wang, Y., 2025. Data for compensational timescale (Tc) analysis under fast cyclic forcing in numerical experiments. https://doi.org/10.5281/zenodo.17008382.

Wang, Y., Abels, H.A., 2025. Alluvial stratigraphic response to abruptly increasing and variable sediment supply: insights from stratigraphic forward modeling. Geophys. Res. Lett. 52, e2025GL115985. https://doi.org/10.1029/2025GL115985.

Wang, Y., Baars, T.F., Storms, J.E.A., Martinius, A.W., Gingerich, P.D., Abels, H.A., 2024. Long-eccentricity pacing of alluvial stratigraphic architecture in the Eocene Bighorn Basin, Wyoming, USA. Geology. 52 (8), 588–593. https://doi.org/10.1130/G52131.1.

Wang, Y., Baars, T.F., Storms, J.E.A., Martinius, A.W., Gingerich, P.D., Chmielewska, M., Buckley, S.J., Abels, H.A., 2023. Lateral and vertical characteristics of floodplain aggradation cycles in the lower eocene Willwood Formation, Bighorn Basin, Wyoming, USA. Geol. Soc. Am. Bull. 136 (5–6), 2568–2581. https://doi.org/10.1130/B36908.1.

Wang, Y., Storms, J., Martinius, A., Karssenberg, D., Abels, H., 2020. Codes and data for "evaluating alluvial stratigraphic response to cyclic and non-cyclic upstream forcing through process-based alluvial architecture modelling". https://doi.org/10.4121/uuid:0fdf13ef-3809-4eed-bb7a-ba8f3b8208aa.

Wang, Y., Storms, J.E.A., Martinius, A.W., Karssenberg, D., Abels, H.A., 2021. Evaluating alluvial stratigraphic response to cyclic and non-cyclic upstream forcing through process-based alluvial architecture modelling. Basin Res. 33, 48–65. https://doi.org/10.1111/bre.12454.

Wang, Y., Straub, K.M., Hajek, E.A., 2011. Scale-dependent compensational stacking: an estimate of autogenic time scales in channelized sedimentary deposits. Geology. 39, 811–814. https://doi.org/10.1130/G32068.1.

Weisberg, S., 2005. Applied linear regression. Wiley Series in Probability and Statistics, 3rd ed. Wiley-Interscience, Hoboken, N.J.. https://doi.org/10.1002/0471704091

Whipple, K.X., Parker, G., Paola, C., Mohrig, D., 1998. Channel dynamics, sediment transport, and the slope of alluvial fans: experimental study. J. Geol. 106, 677–694. https://doi.org/10.1086/516053.

Zhang, J., Jiang, Z., Liang, C., Baars, T.F., Wang, Y., Abels, H.A., 2022. Astronomical forcing of meter-scale organic-rich mudstone–limestone cyclicity in the Eocene Dongying sag, China: implications for shale reservoir exploration. Am. Assoc. Pet. Geol. Bull. 106, 1557–1579. https://doi.org/10.1306/02072220103.